UCLA
UCLA Previously Published Works

Title

Highly dispersed Pt atoms and clusters on hydroxylated indium tin oxide: a view from first-principles calculations

Permalink

Journal

ISSN

Authors

Kumari, Simran
Sautet, Philippe

Publication Date

DOI

Supplemental Material

Peer reviewed

Highly dispersed Pt atoms and clusters on hydroxylated indium tin oxide: A view from first-principles calculations

Simran Kumari[a] and Philippe Sautet*[a,b]

[a] Chemical and Biomolecular Engineering Department, University of California, Los Angeles, Los Angeles, CA 90095, USA

[b] Chemistry and Biochemistry Department, University of California, Los Angeles, Los Angeles, CA 90095, USA

ABSTRACT:

Supported single-atom and small cluster catalysts have become highly popular in heterogeneous catalysis. These catalysts can maximize the metal atom utilization while still showcasing superior catalytic performance. One of the main challenges in producing these small cluster catalysts is their low binding strength with the support, which causes these
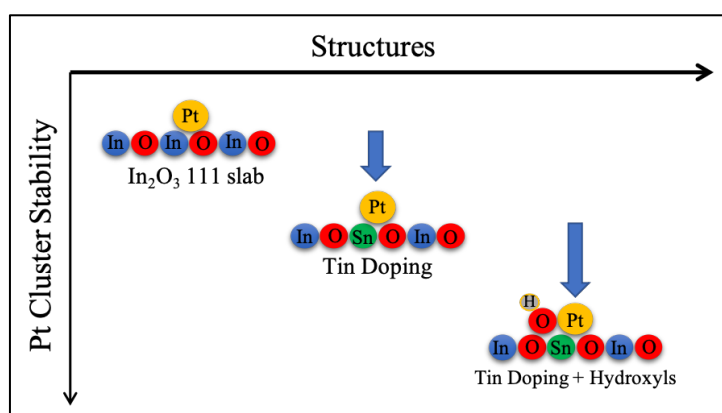
small clusters to sinter into larger nanoparticles. We have used first-principles simulations to study small Pt_n (n: 1,2,3) clusters on Indium Oxide, Tin doped Indium Oxide, and hydroxylated Tin doped Indium Oxide. We report that the Pt_n cluster is stabilized in the presence of Tin and that this is especially the case for Pt- single atom on hydroxylated Indium Tin Oxide support, which are anchored to the support via the hydroxyl group. On this support, the Pt single atoms become more stable than Pt_2 and Pt_3 clusters, hence decreasing sintering. These findings provide a promising way to design single-atom catalysts on electrically conducting supports for electrocatalytic applications and to better understand how functional groups on supports can increase the adhesion of cluster catalysts.

INTRODUCTION:

Assembling metal clusters on high-surface-area supports has been extensively explored to achieve high activity and stability in heterogeneous catalysis[1–4]. Other applications of supported metal clusters include nanoscience, information storage, and magnetism[5–9]. Sub-nanometer scale metal clusters present the advantage of an optimal dispersion, where nearly all the atoms present on the surface contribute towards

improving the catalytic activity, which is vital since the active phase is often formed by rare and expensive transition metals such as Pt or Rh[10–12]. Pt-based catalysts have long attracted scientists' attention because of their importance in catalyzing an extensive range of chemical reactions, including emission control of toxic gases, production of chemicals, and energy conversion in fuel cells[13–16]. Theoretical modeling and experimental research on Pt-based catalysts' properties have been extensive[17–20]. Under the regime of supported metal catalysts, the control of the metallic particle size is a fundamental question[21]. The general behavior is that an increase of metallic coordination number, and hence size, improves the stability. Therefore, the small, bare metallic particles tend to sinter into larger ones, leading to a loss of activity and selectivity. As a result, one of the primary barriers to the industrial application of supported metal catalysts is their stability. Scientists have focused on studying the sintering of supported metal catalysts, and a sizeable metal-support interaction has proven to be vital for the stability of heterogeneous catalysts. Sub-nanometer-sized metal particles present specific electronic and chemical properties.[22,23] Hence, understanding the mechanisms that allow small particles' stabilization is crucial for many application fields, including catalysis.

High-surface area supports such as metal oxides have been thoroughly investigated to study their interaction with small metal clusters and have been found to favor small particles kinetically. This approach is used in heterogeneous catalysis, in which the optimal stabilization of small particles by the support is of significant importance to slow down the often-unavoidable sintering into larger particles and the loss of catalytic activity. One way to increase the stability of small metal particles on supports is to increase the adhesion energy between the particle and the support. This can be accomplished by modifying the oxide interfacial properties, such as defect concentration[24,25,26], surface termination, functionalization[27] or reaction conditions[28,29]. Hydroxyls represent one of the most common functional groups, often omnipresent in realistic conditions and essential for metal support interaction[30,31]. Scientists have already noted evidence of enhanced interactions between the supported metals and the hydroxylated metal oxide for Pd/ɣ-Al$_2$O$_3$[31], Pt/Al$_2$O$_3$[32], Co/Al$_2$O$_3$(0001)[33], Rh/ZrO$_2$[34,35], Pt/ TiO$_2$(011)-2x1[36], Ru/ZrO2[37], Pt/TiO$_2$[38], Pd/MgO[40] and Pd/Fe$_3$O$_4$[41] etc. These interactions cause thermal stabilization and hence more durable catalytic activity of the single-atom or, more generally, highly dispersed catalysts. Understanding how the support and its chemical nature control particle stability as a function of size is key to the conscious design of well-controlled, monodispersed, supported catalysts.

In$_2$O$_3$ is a wide band-gap semiconductor used in semiconductor gas sensors[42] and more recently has also been explored as a potential catalyst for CO$_2$ hydrogenation[43,44]. On doping with Sn, it becomes Indium Tin Oxide (ITO(111)), a transparent conducting oxide with optical transparency in the visible range with metal-like conductivity. This material has applications in transparent electrodes for electro-optical displays, e.g., liquid crystal displays and solar cells[45]. Each has been a subject of intensive research and development activities. Sn doped Indium oxide demonstrates high conductivity, crucial for application in electrocatalysis. These properties have incited scientists to investigate these conductive oxides as supports for Pt-metal clusters for electrocatalytic applications in water[46–48], where the surface might be hydroxylated.

In the present paper, we report first-principles DFT calculations of Pt single atom and small clusters supported on the defect-free In$_2$O$_3$(111), Sn-doped In$_2$O$_3$(111), and hydroxylated Sn-doped In$_2$O$_3$(111) surfaces. By analyzing the structural and electronic properties of the metal clusters on the supports, including the detailed sampling of geometric configurations, we provide insights on the metal-support interactions and the effects of hydroxyl groups. We show that H atoms from hydroxyl groups migrate on the cluster and that this is a crucial mechanism to stabilize and anchor the cluster on the support. This effect is proportionally more substantial on Pt single atom, and therefore hydroxylated support better stabilize Pt$_1$ compared to Pt$_2$ or Pt$_3$ clusters, hence hindering sintering. The manuscript is organized as follows: In Sec. II, we present calculation details and the grand canonical methods used in this work. In Sec. III, we discuss in detail the doping of In$_2$O$_3$(111) by Sn to produce the ITO(111) surface, the water adsorption on ITO(111) , and finally, we discuss the structures of Pt$_n$(n=1,2,3) clusters on the three different supports, their stability, and their electronic and structural properties.
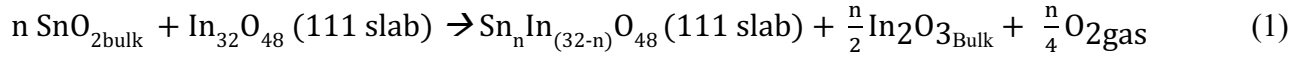
COMPUTATIONAL DETAILS AND MODEL

Total Energy Calculations. All calculations were carried out within the density functional theory framework using the Vienna ab-initio simulation package (VASP). [49,50] The electron-ion interactions are treated using the projector augmented wave (PAW) method.[51] We use the Perdew–Burke–Ernzerhof (PBE) functional to treat the exchange-correlation interactions.[52] The Gaussian smearing method with a smearing of 0.01 eV is used to improve K point convergence. The valence electronic states are expanded in plane-wave basis sets with an energy cutoff of 500 eV. The structures are optimized until the force on each atom is less than 0.01 eV/A$^{\circ -1}$.

Models. The calculated lattice parameters of the bulk Indium Oxide (a= b = c = 10.352Å), which agree well with experiments[53], were used to construct the periodic slabs(111) surface calculations. The $In_2O_3(111)$ unit dimension in the surface plane is 14.63 x 14.63 x 28 Å, including a vacuum region of ~20 Å. The $In_2O_3(111)$ unit cell model contains four tri-layers of O-In-O in that order; each unit cell has 64 Indium atoms and 96 Oxygen atoms, out of which 16 In atoms are 6 coordinated(6c), 48 In atoms are 5c, 48 O atoms are 3c, and other 48 O atoms are 4c. There are 6 non-equivalent In atoms present in the unit cell, and a top view of the slab surface is shown in Fig. 1(a).The different colors represent the non-equivalent metal atoms; light blue : In(6c) bonded with 3O(3c) and 3 O(4c), dark blue : In(6c) bonded with 3O(3c), 2O(4c), red : In(5c) bonded with 3O(3c) and 1O(4c), dark green : In(5c) bonded with 2O(3c) and 3O(4c), lime : In(5c) bonded with 2O(3c) and 2O(4c) and yellow: In(5c) bonded with 1O(3c) and 3O(4c). All of the metal atoms, except the light blue atom, also have 1-O interaction from the second layer and are located at the same z-value on the surface layer. Only the atoms exposed on the surface were shown in the figure. The atoms in the lower layers were removed for clarity. The structures were first studied on 2-Layer slabs, after which the structures with reasonable stability were recalculated on a thicker slab containing four tri-layers. This was done to save computational time and resources. The atoms in the two lower In layers of the 4-layer system and the associated O layers, i.e., the lower half of the slab, were fixed at their bulk positions for all the calculations. The Brillouin-zone (BZ) integration is sampled by adopting the Monkhorst–Pack [54] k-point grids of 5x5x1 for all the surfaces.

Pt-cluster structure exploration. We used the Basin Hopping global optimization method to explore possible adsorption sites for the Pt-SA on the hydroxylated ITO(111) surface and Pt_2 and Pt_3 adsorption structure and site on $In_2O_3(111)$, ITO(111), and Hydroxylated ITO(111). The premise behind the Basin hopping method is very similar to that of canonical Monte Carlo (MC) simulation[55], where the algorithm perturbs the coordinates of the current structure by a random displacement (called perturbation) and then optimizes the new geometry to a local minimum. The optimized structure can be either discarded or accepted, and the algorithm decides this by evaluating the probability that depends on the energy difference between the previously accepted structure and the temperature. The motivation to use basin hopping for our studies was from Sun et al., where they used this method to study Pt_8 cluster on alumina under a pressure of hydrogen.[56]

Energetic Analysis. The doping energy for the Sn doping onto the $In_2O_3(111)$ surface is defined by the following equation:

$$n\ SnO_{2bulk} + In_{32}O_{48}\ (111\ slab) \rightarrow Sn_nIn_{(32-n)}O_{48}\ (111\ slab) + \frac{n}{2}In_2O_{3Bulk} + \frac{n}{4}O_2gas \qquad (1)$$

Hence, the doping energy can be calculated as:

$E(doping) = E\ (Sn_nIn_{(32-n)}O_{48}111\ slab) + \frac{n}{2}E(In_2O_{3Bulk}) + \frac{n}{4}E(O2_{gas}) - nE(SnO_{2Bulk}) - E(In_{32}O_{48}111\ slab)$

Where $E(Sn_nIn_{(32-n)}O_{48}\ 111\ slab)$ is the energy of the slab with n-Sn dopants, $E(In_{32}O_{48}(111\ slab))$ is the energy of the $In_2O_3(111)$ slab, $E(In_2O_{3bulk})$ and $E(SnO_{2bulk})$ are the energies for the bulk structures of In_2O_3 and SnO_2 respectively, $E(O_{2gas})$ is the energy of the gas phase O_2 molecule.

The adsorption energy of H_2O on the ITO(111) surface is defined by:

$G(Adsorption) = E\ (Sn_nIn_{(32-n)}\ O_{48} + pH_2O\ 111\ slab) - E\ (Sn_nIn_{(32-n)}O_{48}\ 111\ slab) - pG(H_2O\ gas)$

Where $G(H_2O\ gas)$ is the Gibbs free energy for gas-phase H_2O and p is the number of H_2O molecules chemisorbed on the surface, $E(Sn_nIn_{(32-n)}\ O_{48} + pH_2O\ 111\ slab)$ is the energy of the slab with p-H_2O molecules, and $E\ (Sn_nIn_{(32-n)}O_{48}\ 111\ slab)$ is the energy of ITO(111) surface slab.

To analyze the evolution of the stability of the clusters on each of the four surfaces, the normalized cluster binding energy, $E_{binding}$, in the presence of the surface was calculated, with the Pt bulk and the bare oxide surface as a reference, following eq:

$$E_{binding} = \frac{E_{nPt + surface} - E_{surface} - E_{Pt-bulk}}{n}$$

Here, $E_{nPt + surface}$ is the energy of the Pt cluster with n Pt atoms on the surface, $E_{surface}$ is the energy of the oxide support and, $E_{Pt-bulk}$ is the energy of Pt-bulk. $E_{binding}$ is positive (meaning less stable) and corresponds to the energy loss, normalized to 1 Pt atom, for the supported cluster compared to Pt bulk.

RESULTS AND DISCUSSION:

Before presenting the results of Pt_n (n = 1,2,3) interaction with the surface of $In_2O_3(111)$, ITO(111), and hydroxylated ITO(111), we first determine the most energetically desirable structure for our ITO(111) surface. To do this, we begin with doping Sn onto each of the non-equivalent sites (Fig. 1(a)). After a

detailed analysis, the Sn prefers to reside in the light blue(6c) and the red(5c) sites and at a vertical z coordinate 0.14 Å higher than that of the In they substitute. We increased the Sn doping concentration from 1.25% (1Sn atom for a 80 atom bilayer slab) to 5% (4Sn atoms for a 80 atom bilayer slab). We observe that as we increase the doping level, the surface energy decreases; hence the substitution of In by Sn stabilizes the surface (SI – Fig-5). We have considered 5% ITO(111) for our studies in this work as it
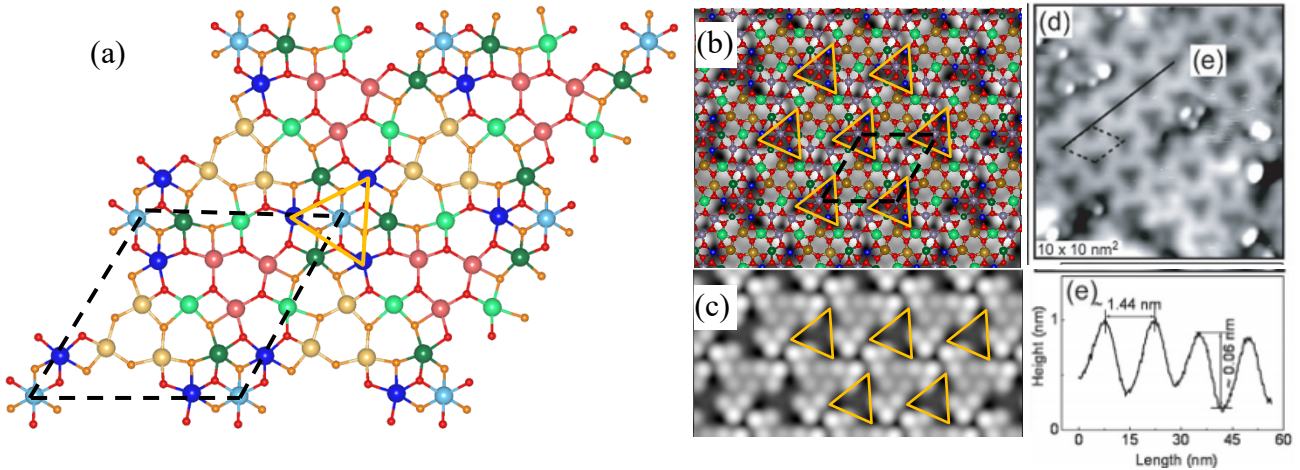

Figure 1:(a) Structure of the first layer of the $In_2O_3(111)$ 2x2 surface. The different color In atoms represent the non-equivalent In atoms (see text). The orange balls are the O atoms that are 3-coordinated and the red balls are the O that are 4-coordinated. (b) and (c): Calculated STM image of the 5% Sn doped $In_2O_3(111)$ surface. In (a) and (b), the black dotted line represents one unit cell and in (a), (b) and (c) the yellow triangles highlight the lower current (dark) regions. d) experimental STM image of the 5% Sn doped $In_2O_3(111)$ surface (I_{tunnel} = 0.4nA and Vsample = +1.7V) from ref 40 (e) topographic profile along the line marked in (d) gives an experimental lattice constant of 14.44Å for the dark areas which is very close to the lattice constant of 14.65Å from our calculations.

has been previously reported to provide an optimum Tin doping level for the highest carrier density[57]. In the case of 5% doping, we find that all Sn atoms prefer to locate in the surface layer. For a four-layer slab, 8 Sn atoms are present, 4 in the top and 4 in the bottom layer. 3 Sn atoms replace the In atoms in the red 5 coordinated sites, and 1 Sn atom replaces the In in the light blue 6 coordinated site. The SI shows detailed results of the different doping energies of all the possible sites (SI – Fig. 3). We also did not observe any dependence of doping energies on the Sn-Sn distance in the slab (SI – Fig. 4). In Figure 1(b) and 1(c), we show the simulated empty state STM image (Vsample = 1.7V) using the p4vasp code alongside the experimental image (Fig. 1(d)) for the Sn doped $In_2O_3(111)$ surface. We observe that the calculated and experimental STM images are very similar with very prominent dark triangular features (marked in yellow on the simulated images of Fig. 1(b) and 1(c)). These black zones correspond to the triangle defined by the In (6c) atoms (blue in Fig. 1(a)), one Sn atoms being at its center (light blue position). The repeat vector for these black features from our simulations (14.65 Å) also compares well with the experimental value (14.44 Å)[58]. The 6 coordinated Indium atoms are saturated, and hence the local density of empty

states is decreased. The slightly brighter points between the dark triangles on the simulated STM image are the Sn atoms in the red positions. The contrast in the STM image is explained by the electronic density of states (DOS) projected on each surface atom of ITO(111) , between the Fermi level and the Fermi level + 1.7 eV (SI Fig. 7(a), (b)): 6-coordinated Sn (light blue) and In (blue) show a very low DOS and hence appear dark in the image, while 5-coordinated Sn (red) provide the largest DOS and appear brightest.

A) H_2O interaction with the ITO(111) surface:

To study the interaction of Pt-clusters with the hydroxylated surface of ITO(111), we first need to resolve the structure of the hydroxylated ITO(111) surface. We performed a series of DFT calculations to determine the adsorbed water structure on the ITO(111) surface to achieve this goal. The first step was to start with the 1-H_2O molecule and study the configurations of both dissociative and molecular adsorptions onto the surface. The supplementary information gives a detailed analysis of the adsorption energies of the different configurations. The calculations show that molecular adsorption of water molecule takes place via their oxygen atom, O_W, to the unsaturated In (5c) sites, and in the case of dissociative adsorption, the proton converts an O(3c) surface oxygen, O_S, to a hydroxyl (O_SH). The remaining O_WH group from the water molecule takes either an on-top or a bridging position at the In(5c) sites. Dissociative adsorption is preferred over molecular adsorption by 0.23eV. In the most favorable configuration (Fig. 2(a)), the proton adsorbs on one of the three O(3c) binding to two In(6c) and one In(5c). The remaining O_WH group adsorbs in a bridging position between the two In(5c) closest to the O_SH group. Subsequently, a second, third and fourth water molecule was added to the surface unit cell; in this case, only a handful of adsorption sites were considered depending on the adsorption energies they had with respect to 1-H_2O molecule adsorption. In the most favorable configurations, the water molecule was dissociatively adsorbed until 2-H_2O adsorption. After this, any additional water molecule would be molecularly adsorbed. The two hydroxyls adsorb to two of the three symmetrically equivalent sites (Fig. 2(b)). However, the third site favors the molecular adsorption of H_2O over dissociative adsorption (Fig. 2(c)). The fourth H_2O took the second most favorable site for molecular adsorption (Fig. 2(d)). We can notice a direct H-bonding between the dissociated H_2O and nearby molecularly adsorbed H_2O. The direct adsorbate-adsorbate interaction contributes to the stabilization of partially dissociated H_2O over completely dissociated and intact H_2O molecules. This behavior is also observed in methanol adsorption on rutile $TiO_2(110)$[59].

The binding energy per molecule decreases slightly from -1.02 to -0.97 to -0.90 and -0.88 eV when going from one to two to three and four water molecules, respectively. The decrease in the binding energy can

be attributed to the slight, surface-mediated repulsion between the molecules due to the surface re-relaxation. This re-relaxation contributes to the binding energy and affects the first adsorbate to the fullest, after which it starts reducing. This phenomenon is of general importance for oxides[59,60]. On the surface stability diagram of Fig. 2(e), the pink shaded region corresponds to the chemical potential range for water where the surface would only contain hydroxyls but no water molecules. As we move beyond the pink region, we observe that any additional water molecule would undergo molecular adsorption. Hence, the maximum hydroxyl coverage on the ITO(111) surface is 1.1 hydroxyl per unit area of the cell. The vertical black dotted line marks the water chemical potential at room temperature and standard pressure.[61] We also studied solvation effects on water adsorption by including an explicit solvent and found that the conclusions are not qualitatively modified.

Our primary motivation to resolving the structure of hydroxyl/water adsorption on the ITO(111) surface is that when we move forward to study the Pt-cluster adsorption on the hydroxylated surface, the hydroxyls will become very important as they might provide extra anchoring to the Pt-clusters. On the other hand, the intact water molecules are less critical because they do not have any strong chemical interactions with the Pt-cluster and can also move around on the surface upon Pt-cluster adsorption. Hence, keeping this in
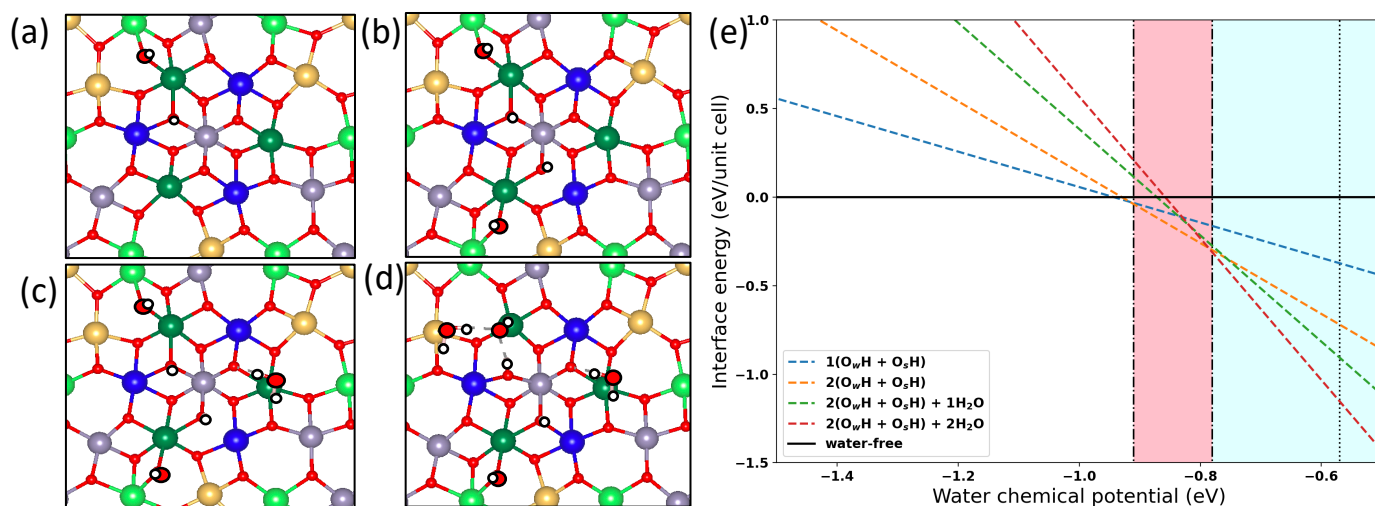

Figure 2: (a),(b),(c),(d) gives the best structures for H2O adsorption on the ITO(111) surface.(a) $1H_2O$ dissociative adsorption (b) $2H_2O$ dissociative adsorption (c) $3H_2O$: $2H_2O$ dissociative adsorption + $1H_2O$ molecular adsorption (d) $4H_2O$: $2H_2O$ dissociative adsorption +2 H_2O molecular adsorption. The atoms with black border represent the atoms from water (e) The phase diagram at constant room temperature. The dotted line is the liquid water chemical potential at room temperature and 1atm pressure[3]. The red shaded region is the region where the hydroxylated surface is stable, and the blue shaded region is where the molecular + dissociative adsorption is more stable.

mind, we move forward with the $4H_2O$ on ITO(111) surface as it provides the maximum number of hydroxyl groups, and even if additional water molecules could be molecularly adsorbed on the surface.

B) Pt_n (n=1,2,3) on the In_2O_3(111) and ITO(111) surfaces:

Pt-SA: We systematically probed all non-equivalent adsorption sites on the In_2O_3(111) and ITO(111) surfaces for Pt-Single atoms (SA). In total, we found six stable sites for the Pt-SA adsorption. These different sites for In_2O_3(111) and ITO(111) are shown in the SI (SI – Fig. 9,10). Figure-(3) shows the adsorption energy for every site, while the structure of the best site is shown in figure 4 (a) and (d), for In_2O_3(111) and ITO(111) , respectively. In the case of In_2O_3(111), site 3 is the most stable adsorption site for the Pt-SA, where Pt is located 1.20 Å above the top layer of the surface and is interacting with one In(6), two In(5), and two O atoms (Pt-O bond distances of 2.01 and 2.05 Å which is very close to the bond distances observed in PtO_2, 1.97Å). A significant restructuring of the oxide support occurs with the displacement of each of these two O atoms by 1.06 Å, including a vertical move by 0.62Å, breaking two In(6)-O bonds and forming two Pt-O bonds. The adsorption of Pt on In_2O_3 is hence markedly reactive, Pt inserting into two In(6)-O bonds. On the ITO(111) surface, Pt is similarly located 1.16 Å above the plane of the surface, but the adsorption site differs: the most favorable site is site 1, Pt interacting with two nearby Sn atoms and one In, displacing the O atom between these 3 atoms by 2 Å. The Pt-O bond distance is 1.99 Å, the Pt-Sn distances are 2.6 and 2.52 Å, and the Pt-In distance is 2.63 Å. The oxide surface is again markedly modified, with one In(5)-O and one Sn-O bond broken.

One key aspect to explain the change in the adsorption site preference is the very different work functions for the two supports: In_2O_3(6.12eV) and ITO(111) (4.46eV). This difference arises from the filling in ITO(111) of bands initially vacant in In_2O_3 since the Sn atom substituting In has one more electron. On In_2O_3, the Pt atom is, depending on the binding site, neutral (as evaluated from the Bader charge) or slightly electronically depleted by transfer to the support (by 0.3e at most on-site 4). On ITO(111), and its much lower work function, the electronic transfer is very different, and Pt is generally electronically enriched. Site 3 (Pt atom attached to 1 In(6), 1 In(5) and 1 Sn(5c)) and site 4 (Pt atom attached to 1 In(6), 1 In(5), and 1 Sn(6c)) however, do not follow this trend and keep a small depletion on Pt. As a consequence, their adsorption energy on ITO(111) is significantly weakened. The best binding site for Pt shifts to site 1, which is well adapted for a transfer (0.30e) from ITO(111) to Pt due to the strong interactions with the nearby Sn atoms. The DOS of the most energetically favored structures are given in SI-Fig. (12c,12d). We observe that for Pt-SA on In_2O_3(111), the Fermi energy moves towards the conduction band, whereas, for Pt-SA on ITO(111) , the Fermi energy moves towards the valence band. This movement of Fermi level confirms that the transfer of electrons occurs from Pt(4d) to In_2O_3(111) surface and from ITO(111) surface to Pt(4d), as discussed above. When we dope 4 Sn in the In_2O_3(111) surface, the four extra electrons from the Sn do not distribute uniformly but accumulates in the area

surrounding the doping site. The heterogeneity of electron distribution in the ITO(111) surface causes the charge to play a role in the Pt adsorption, inducing the Pt SA to choose a site that will help Pt gain electrons from the ITO(111) surface. Hence, both the adsorption environment and the charge distribution play a significant role in the Pt-SA adsorption. The adsorption energies of all the systems are positive with respect to bulk, which means that the Pt atoms in the bulk phase are more stable than the Pt atom adsorbed on the supports.

Another aspect to consider is if the Pt-SA would displace the Sn atoms leading to formations of Sn defect sites. This can be simulated when we consider reactions between the ITO(111) slab, In_2O_3 bulk, and Pt-bulk in an oxygen rich environment, leading to $PtSn_7In_{56}O_{96}$ (with one Pt substituting an Sn) and ITO(111) bulk. We observe that the Pt-SA will stay as a single atom on the surface until an oxygen chemical potential of -1.48eV, and as we increase the oxygen chemical potential, the Pt-SA would displace Sn and interact directly with the surface through the defect site (SI-Section:5)
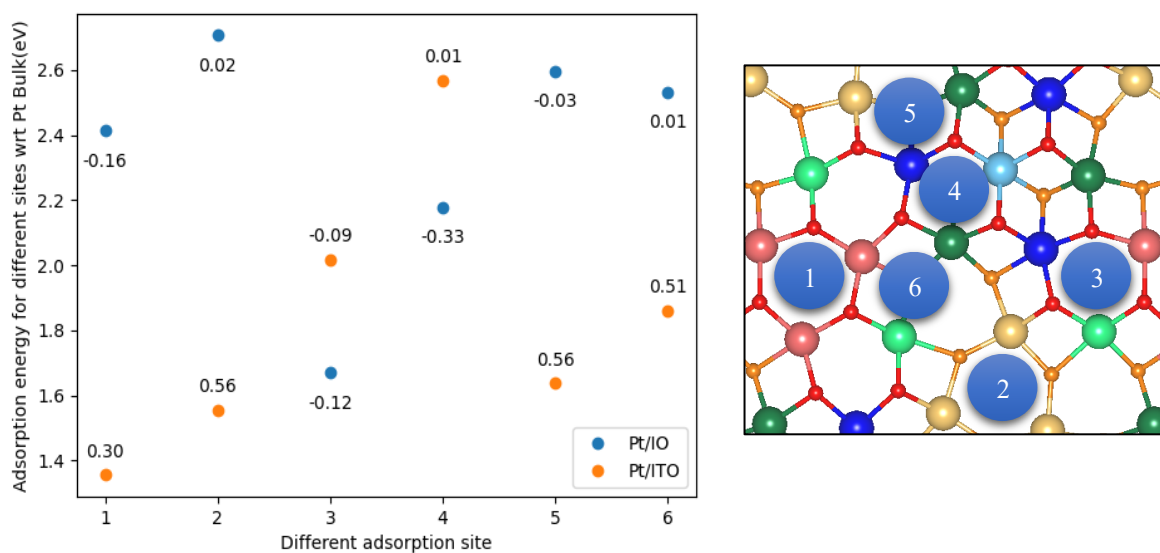

Figure 3: Adsorption energy of Pt-SA adsorption on the different sites on $In_2O_3(111)$ and ITO(111) alongside the different sites shown on the surface. The different sites ae marked on the surface in the SI-Fig. (8, 9). The bader charges are given on the respective points for the different Pt adsorption sites. It is calculated as (electrons on Pt – 10). Hence, positive means higher electron density-gain in charge from the support whereas negative means lower charge density- loss in charge to the support. (In case of ITO(111) red and light blue sites are Tin)

Pt₂/Pt₃: To explore the possible configurations of the Pt-dimer and trimer on the $In_2O_3(111)$ and ITO(111) surfaces, we employed the basin hopping method. The procedure generated a total of around 300 optimized structures in both cases. We concluded our basin hopping algorithm once all the sites on the slab were covered, and no new structure was found for ~100 steps. We have presented a few of the best structures for both the dimer and trimer cases, along with their relative energies in the SI-Section-7. On $In_2O_3(111)$, the dimer prefers the triangular region containing the In(6c) atoms (marked with a yellow line

in Fig. 1(a), In(6c) being blue). The preferred sites for Pt-SA (site-3 and site-4) are also close to this triangular region. Three oxygen atoms are displaced, five In-O bonds are broken (four In(6)-O and one In(5)-O), and four Pt-O bonds are created, one O bridging two Pt atoms. Hence the dimer adsorption involves a rearrangement of the support. In the case of the trimer, even though the most energetically favored structure does not sit in the triangular region, 4 out of the 5 best structures (SI-Fig 14) have the Pt$_3$ cluster interacting with the specific triangular region. On the most stable structure of Fig 4c, the Pt$_3$ structure is gaining stability by its interaction with the neighboring 3 In(5c) (2.67 Å) and 3 O (1.93 Å) and sits on the site in a perfect triangular shape (Pt-Pt = 2.61 Å), displacing three O atoms. Again, a substantial reconstruction of the O atoms occurs, breaking two In(5c)-O bond for each involved O. In contrast, on ITO(111) , the dimers/trimers do not prefer the triangular region but interact more favorably with the Sn
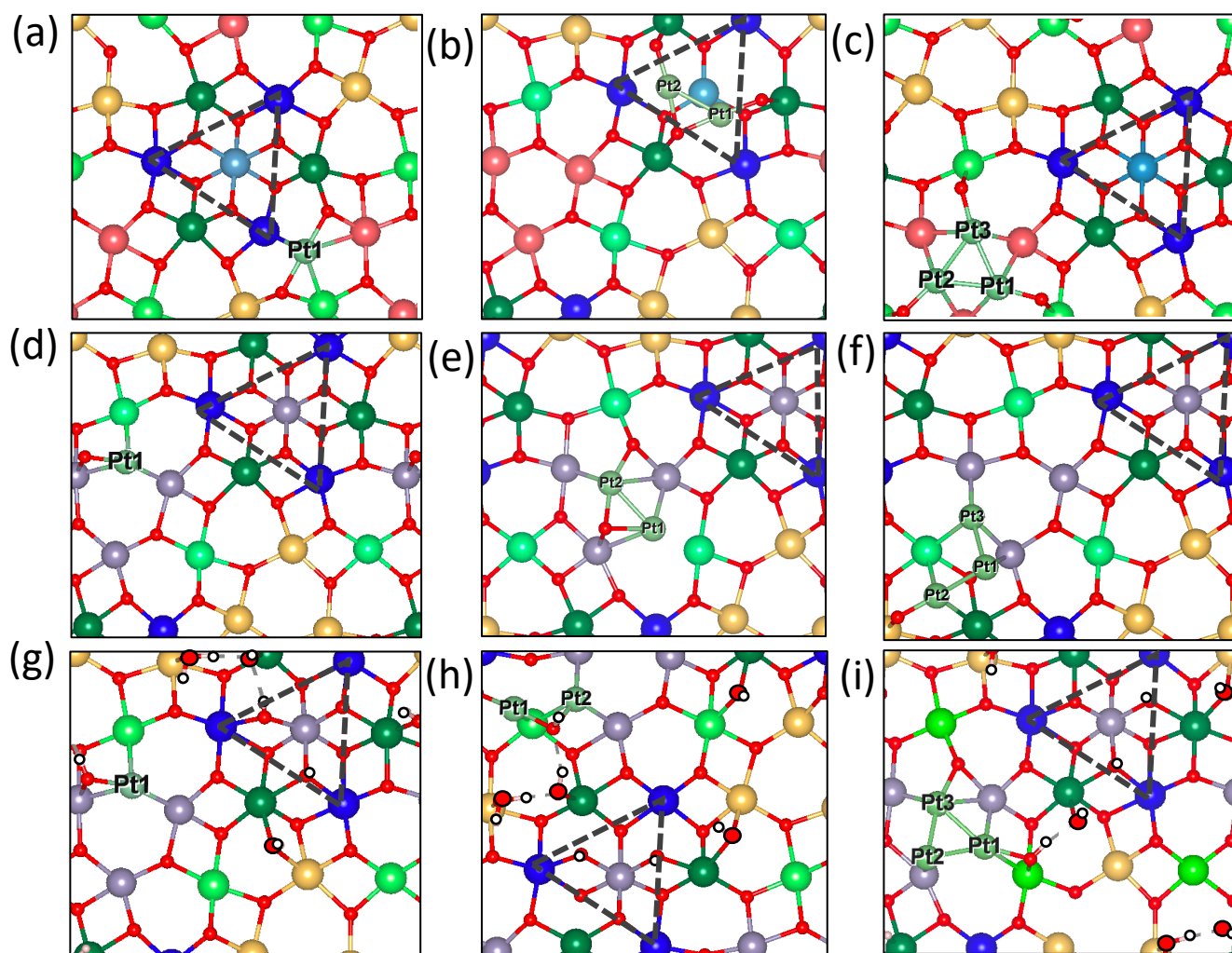

Figure 4: Pt-SA, dimer, trimer respectively on (a), (b), (c) In$_2$O$_3$(111) (d), (e), (f) ITO(111) and (g), (h), (i) on hydroxylated ITO(111) .

atoms in between these triangular regions for the same reason the Pt-SA did. The Bader charge analysis shows that the dimer and trimer on $In_2O_3(111)$ lose a total electronic population of 0.62 and 0.06 e, respectively. Whereas in the case of ITO(111) , the dimer and trimer gain a total electronic population of 0.27 and 0.70 e, respectively. This loss or gain in the electronic population is again in line with the work functions of these materials, as discussed above. The adsorption energy per Pt-atom on $In_2O_3(111)$, referenced to Pt bulk, stabilizes from +1.67eV to +1.45eV to +1.21eV as we move from Pt-SA to dimer and trimer, hence slowly trending towards the bulk value of zero. Similarly, for the case of ITO(111) , the adsorption energy of Pt-atom, reference to Pt-bulk, stabilizes from +1.36eV to +1.29eV to +1.19eV when we move from Pt-SA to dimer to trimer. This implies that the Pt-SA would sinter to a larger cluster or particles on $In_2O_3(111)$ and ITO(111). We also studied the stabilization of the dimer and trimer on the surface relative to 2 and 3 separated adsorbed Pt-atoms. The energy of the dimer and trimer were 0.83eV and 0.57eV lower than that of their fragmented counterparts for $In_2O_3(111)$, verifying the better stability of these clusters on the $In_2O_3(111)$, with respect to the SA.

C) Pt$_n$ (n: 1,2,3) on hydroxylated ITO(111) surface:

Finally, we studied the effects of surface hydroxyls and water molecules on the adsorption of the Pt clusters. We used the $4H_2O$-ITO(111) surface, including two dissociated water molecules (hence 4 surface OH groups) and two molecularly adsorbed waters, as our starting point, and we introduced the Pt-clusters. We employed the basin hopping approach for finding the best possible adsorption site and structure for our Pt – structures. The most important point to remember in this case is that the -OH/H_2O groups can move around the support to find a new binding site depending on where the Pt-cluster prefers to bind. We considered the possibility of -OH/-H/-H_2O migrations throughout the surface and reverse spillover of these groups onto the Pt-clusters. Ultimately, after around 350 local optimizations, we were able to find the putative global minimum structures for our Pt-SA, dimer, and trimer structures, shown in fig. 4 (g), (h), (i). The few of the best structures for Pt-SA, dimer, and trimer are given in the supplementary information along with their relative energies (SI Section 8). Pt-SA is best located in the Sn rich area of the surface,
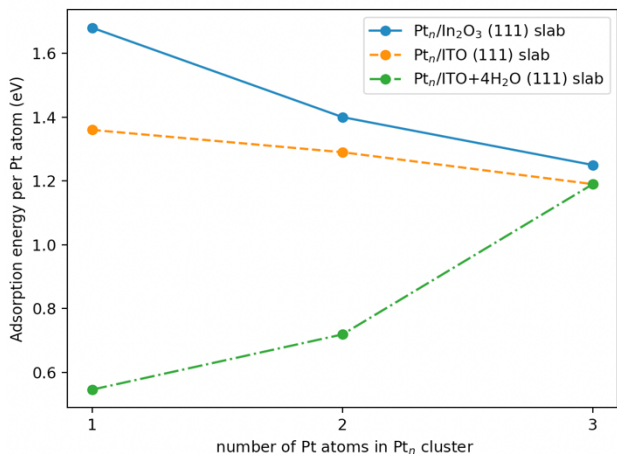
Figure 5: Adsorption energy of Pt-SA, dimer, trimer on different supports wrt Pt-Bulk.

similarly to the non-hydrated case, and it displaces an O atom to interact with that O atom, two Sn and one In. In addition, that O atoms become protonated, forming an OH group bridging Pt and Sn. The low coordinated bridging O is markedly stabilized by the interaction with the proton, explaining the more stable energy of the Pt-SA on the hydroxylated ITO(111) surface. The Pt-SA atom moves farther from the surface compared to that of the non-hydroxylated ITO(111) surface by 0.08 Å. The dimer maintains one Pt in the position of the SA and adds a second Pt bridged by the OH group, with a Pt-Pt bond distance of 2.74 Å (2.5% shorter than in Pt bulk). The trimer also sits close to the tin atoms, interacting with 3 Sn sharing 1 O and one OH with neighboring In. The Pt trimer has an average Pt-Pt bond distance of 2.62Å (6.8% shorter than in Pt bulk). A comparison of adsorption energies of all the structures of Pt-SA, dimer, trimer for the In_2O_3(111), ITO(111), and hydroxylated-ITO(111) supports of is given in Figure-5. We observe that the presence of water/hydroxyls stabilizes all three Pt-structures compared to In_2O_3(111), and ITO(111), but the stabilization per Pt atom is much larger for Pt_1, followed by Pt_2, and is very small on Pt_3. Consequently, the Pt-SA becomes more stable than the dimer and trimer. The adsorption energy per Pt-atom on the hydroxylated surface is destabilized from 0.52eV to 0.71eV to 1.20eV when going from Pt_1 to Pt_2 and Pt_3. Although the adsorption energy of the Pt-SA is still slightly positive, indicative of a global small thermodynamic trend to sintering, the nucleation of a larger cluster is kinetically not favorable. This sintering resistant adsorption of Pt-SA on the $4H_2O$-ITO(111) can be attributed to the strong anchoring provided by the nearby hydroxyl. This observation is also corroborated by Weber et al[48] in their study of size selected Pt_n clusters (n=1-14) deposited on ITO(111) , where they suggested from their electrochemical study that even at a high Pt_1 coverage (0.1 monolayer) a substantial fraction of the deposited Pt_1 remain isolated and do not sinter into larger Pt-clusters. In the case of the non-hydroxylated ITO(111) surface, the surface restructuring upon Pt interaction displaces a O atom, putting it in a bridge position between Sn and Pt. This low coordination O atom is reactive (electronic depletion of 0.23e) and water molecules are introduced on the surface this O gets protonated, which helps stabilizing the Pt atom. This is also visible through the density of states presented in Fig 6(c) and 6(d), where we observe well defined Pt states that primarily mix with orbitals of the bridging O and of Sn1, and
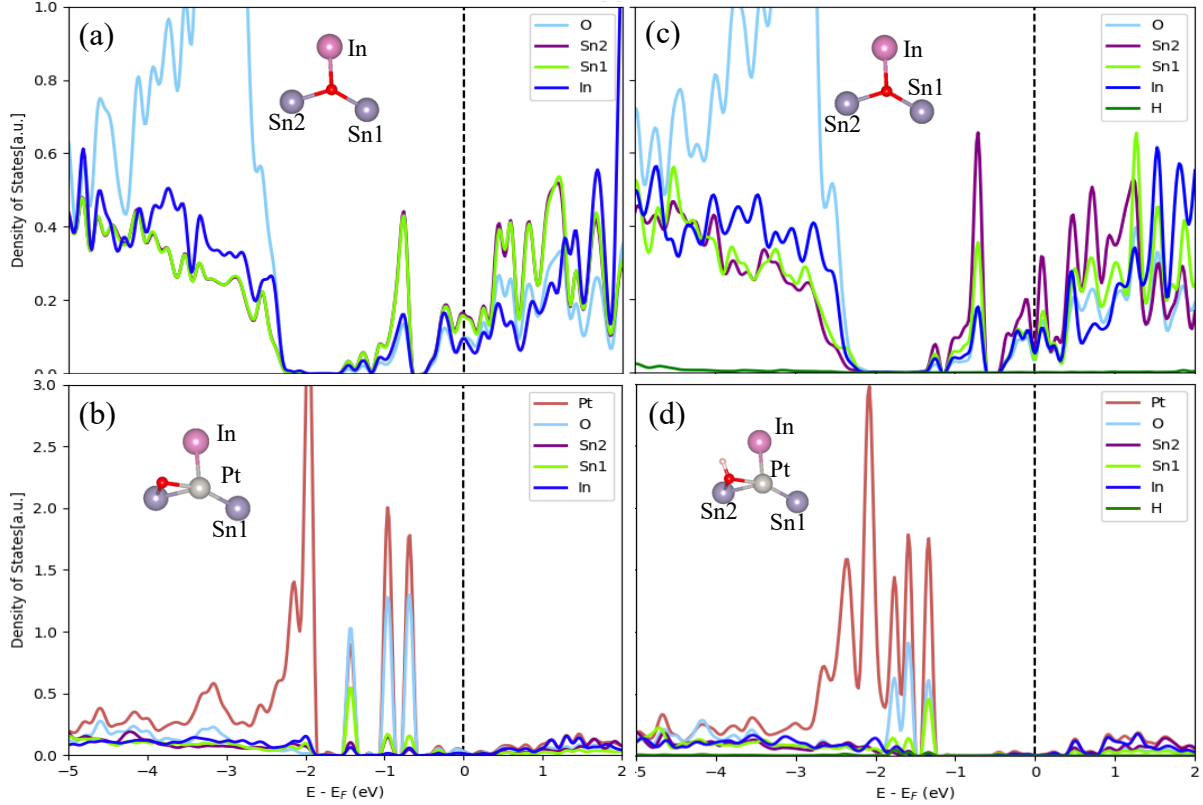
Figure 6: Atom-resolved density of states projected on the atoms interacting with the Pt single atom for (a) ITO(111) (b) ITO(111)+4H$_2$O before Pt deposition and (c) Pt-SA/ITO(111) (d) Pt-SA/ITO(111)+4H$_2$O after Pt deposition, including then the projection on the Pt atom in red.

where these states are lying lower in energy into the valence band of the hydroxylated system than in the case of the non-hydroxylated system. In the case of the dimer, we observe the complete migration of an OH from the oxide support to the metal, also called reverse-spillover, which is a feature that is also observed on Pt/Al$_2$O$_3$. Whereas for the trimer, we see the interaction with a nearby -OH group, but the energy stabilization compared to the non-hydrated ITO(111) is very modest. Spillover of OH is hence of utmost importance for the stabilization of highly dispersed Pt clusters on hydroxylated ITO(111). The Bader charge analysis shows that all the three Pt clusters gained charge from the 4H$_2$O-ITO(111) surface. The Pt-SA, dimer, and trimer gained an electronic population of 0.33, 0.15, and 0.51 e, respectively.

An influence of surface hydroxyl groups on the binding of single atoms on oxide surfaces was also observed in the literature and the authors provided three possible reasons for the stability:

1) An enhanced binding of adatoms to surface sites adjacent to hydroxyl groups as observed in the case of Pd/ɣ-Al$_2$O$_3$[31], Pt/Al$_2$O$_3$[32], Co/Al$_2$O$_3$(0001)[33], Rh/ZrO$_2$[34,35], Ru/ZrO2[37], Pt/TiO$_2$[38], Pd/MgO[40], Pd/Fe$_3$O$_4$[41]. This metal - hydroxyl interaction can be different for different adatoms

and might in some cases lead to decreased stability and hence increased mobility and sintering as observed in Au/TiO$_2$(110)[62].

2) The hydroxyls can provide excess oxygen to oxidize the metal adatom leading to formations of MO$_x$ type moieties as observed in Pt/TiO$_2$[38]and Ru/ZrO$_2$[37].

3) The increased stability of small clusters can also be caused by the higher surface diffusion barriers of the metal atoms, therefore reducing the mobility and the sintering effects. This diffusion barrier is the direct consequence of the high hydroxyl coverage on the support. As the metal coverage is increased the hydroxyl coverage decreases because of the reverse spillover of -H/-OH atoms from the support to the cluster. This causes an increase in the mobility of the metal atoms followed by sintering which is observed in Pt/ TiO$_2$(011)- 2x1[36]. In this case, oxide supports which inherently have a higher hydroxyl coverage and binds them more strongly (not allowing reverse spillovers to the cluster) might be a strategy to stabilize the small metal clusters and avoid sintering.

In our work, even with a very low and constant hydroxyl coverage across the different cluster sizes, we were able to observe a large stabilization of Pt-SA due to the adjacent hydroxyl group. This was caused by the marked reconstruction of the support due to interaction with the Pt atom, which displaced the nearby oxygen that was then stabilized by proton spillover from the support in the case of hydroxylated ITO(111). Static calculations that do not include such spillover motions would give a much weaker interaction (by ~0.8 eV) for Pt-SA. This phenomenon where the oxide reconstruction leads to the formation of an hydroxyl group interacting with the single atom/small cluster and stabilizing it has not been previously reported to our knowledge.

CONCLUSION:

We used first-principles DFT calculations to determine the best doping sites and structure for the Sn doped Indium Oxide(111) surface. Sn atoms substitute In atoms and prefer to reside in the surface layer. Two locations for Sn are seen. The Sn atom can be 6 coordinated with O, in the middle of a triangle of 6 coordinated In atoms. In this case, Sn is saturated, does not show in the STM image, and is not reactive. Alternatively, Sn can be 5 coordinated with O, bright in the STM image and reactive with Pt clusters. We also study the ITO(111) surface after exposure to water at room temperature. ITO(111) is one of the most frequently used materials in flat panel displays; despite its popularity, very little is known about its reactivity with water. From our calculations, the maximum hydroxyl coverage is relatively low, with only 1.1 hydroxyl per nm^2. After which, the H$_2$O molecules tend to stay in the molecular form on the surface.

The four hydroxyls bridge 5-coordinated In atoms at pairs of symmetrically equivalent sites. Even though a third pair of symmetrically equivalent site was present, the third H_2O chooses to adsorb molecularly and not dissociatively. This, therefore, means the hydroxyl coverage is not site-dependent but surface dependent. The stability of intact water molecules over hydroxyls with increasing water coverage can be attributed to the attractive adsorbate - adsorbate interaction (in this case, the H-bonding) and the repulsive substrate mediate adsorbate-adsorbate interaction.

The adsorption of Pt clusters on the In_2O_3, ITO(111), and 4-H_2O-ITO(111) surface is markedly reactive, displacing O atoms to form Pt-In or Pt-Sn bonds. The adsorption site on In_2O_3(111) involves the electronically deficient area which encompasses the In(6c) and In(5c) whereas on ITO(111) the Pt adsorbs on the electronically enriched site encompassing the Sn(5c). This change in adsorption site is attributed to the different work functions and the heterogeneity in the two surface's charge density. This heterogeneity is the direct consequence of the Sn-doping in the In_2O_3(111) surface that injects 4 electrons in the surface unit cell. On ITO(111) , Pt clusters adsorb preferentially on the reactive 5-coordinated Sn atoms, also bridging with neighboring unsaturated In atoms and displacing a O atom. The adsorption energy per Pt atom is decreased as the number of Pt atoms is increased in the adsorbed clusters due to the formation of the strong Pt-Pt bonds in the case of In_2O_3(111) and ITO(111) , which thus tells us that the Pt-SA is not globally stable and can sinter to a dimer, trimer and eventually to bigger Pt-clusters. This sintering behavior is modified by introducing hydroxyls/water on the surface of ITO(111) . The Pt-clusters interaction with hydroxyls and water stabilizes the Pt-SA and the dimer by ~0.5 eV while the trimer is not significantly stabilized. This results in a considerable energy cost to form the trimer on the hydrated ITO(111) surfaces (0.6 eV) such that sintering becomes more difficult to sinter and that Pt-SA can remain metastable at moderate temperature.

Our present results serve as a starting point for our future study of small Pt clusters on the hydroxylated ITO(111) surface and their electrocatalytic properties.

CONFLICTS OF INTEREST:

There are no conflicts to declare.

REFERENCE:

1   L. Liu and A. Corma, *Chem. Rev.*, 2018, 118, 4981–5079.

2   M. Boudart, *Chem. Rev.*, 1995, **95**, 661–666.

3   R. Schlögl, *Angew. Chemie - Int. Ed.*, 2015, 54, 3465–3520.

4   P. Munnik, P. E. De Jongh and K. P. De Jong, *Chem. Rev.*, 2015, 115, 6687–6718.

5   F. C. Meunier, *ACS Nano*, 2008, **2**, 2441–2444.

6   M. Haruta, *Catal. Today*, 1997, **36**, 153–166.

7   H. J. Freund, *Surf. Sci.*, 2002, **500**, 271–299.

8   J. Bansmann, S. H. Baker, C. Binns, J. A. Blackman, J. P. Bucher, J. Dorantes-Dávila, V. Dupuis, L. Favre, D. Kechrakos, A. Kleibert, K. H. Meiwes-Broer, G. M. Pastor, A. Perez, O. Toulemonde, K. N. Trohidou, J. Tuaillon and Y. Xie, *Surf. Sci. Rep.*, 2005, 56, 189–275.

9   G. A. Somorjai, H. Frei and J. Y. Park, *J. Am. Chem. Soc.*, 2009, 131, 16589–16605.

10   A. Wang, J. Li and T. Zhang, *Nat. Rev. Chem.*, 2018, 2, 65–81.

11   Y. Tang, C. Asokan, M. Xu, G. W. Graham, X. Pan, P. Christopher, J. Li and P. Sautet, *Nat. Commun.*, 2019, **10**, 1–10.

12   Q. Liu and Z. Zhang, *Catal. Sci. Technol.*, 2019, **9**, 4821–4834.

13   Y. Zhai, D. Pierre, R. Si, W. Deng, P. Ferrin, A. U. Nilekar, G. Peng, J. A. Herron, D. C. Bell, H. Saltsburg, M. Mavrikakis and M. Flytzani-Stephanopoulos, *Science (80-.).*, 2010, **329**, 1633–1636.

14   N. Jung, D. Y. Chung, J. Ryu, S. J. Yoo and Y. E. Sung, *Nano Today*, 2014, 9, 433–456.

15   J. Lin, X. Wang and T. Zhang, *Cuihua Xuebao/Chinese J. Catal.*, 2016, 37, 1805–1813.

16   Y. Lykhach, A. Bruix, S. Fabris, V. Potin, I. Matolínová, V. Matolín, J. Libuda and K. M. Neyman, *Catal. Sci. Technol.*, 2017, 7, 4315–4345.

17   K. Ding, A. Gulec, A. M. Johnson, N. M. Schweitzer, G. D. Stucky, L. D. Marks and P. C. Stair, *Science (80-.).*, 2015, **350**, 189–192.

18   A. Bruix and K. M. Neyman, *Catal. Letters*, 2016, **146**, 2053–2080.

19   Z. Yan, Z. Xu, J. Yu and M. Jaroniec, *Environ. Sci. Technol.*, 2015, **49**, 6637–6644.

20   A. S. Crampton, M. D. Rötzer, C. J. Ridge, F. F. Schweinberger, U. Heiz, B. Yoon and U. Landman, *Nat. Commun.*, 2016, **7**, 1–12.

21   C. Dong, Y. Li, D. Cheng, M. Zhang, J. Liu, Y. G. Wang, D. Xiao and D. Ma, *ACS Catal.*, 2020, **10**, 11011–11045.

22   S. Vajda, M. J. Pellin, J. P. Greeley, C. L. Marshall, L. A. Curtiss, G. A. Ballentine, J. W. Elam, S. Catillon-Mucherie, P. C. Redfern, F. Mehmood and P. Zapol, *Nat. Mater.*, 2009, **8**, 213–216.

23   S. I. Sanchez, L. D. Menard, A. Bram, J. H. Kang, M. W. Small, R. G. Nuzzo and A. I. Frenkel, *J. Am. Chem. Soc.*, 2009, **131**, 7040–7054.

24   J. Zhang, X. Wu, W. C. Cheong, W. Chen, R. Lin, J. Li, L. Zheng, W. Yan, L. Gu, C. Chen, Q. Peng, D. Wang and Y. Li, *Nat. Commun.*, 2018, **9**, 1–8.

25   J. Wan, W. Chen, C. Jia, L. Zheng, J. Dong, X. Zheng, Y. Wang, W. Yan, C. Chen, Q. Peng, D. Wang and Y. Li, *Adv. Mater.*, 2018, **30**, 1705369.

26   B. Qiao, J. X. Liang, A. Wang, C. Q. Xu, J. Li, T. Zhang and J. J. Liu, *Nano Res.*, 2015, **8**, 2913–2924.

27   C. Mager-Maury, C. Chizallet, P. Sautet and P. Raybaud, *ACS Catal.*, 2012, **2**, 1346–1357.

28   Y. Tang, C. Asokan, M. Xu, G. W. Graham, X. Pan, P. Christopher, J. Li and P. Sautet, *Nat. Commun.*, 2019, **10**, 1–18.

29   R. Lang, W. Xi, J. C. Liu, Y. T. Cui, T. Li, A. F. Lee, F. Chen, Y. Chen, L. Li, L. Li, J. Lin, S. Miao, X. Liu, A. Q. Wang, X. Wang, J. Luo, B. Qiao, J. Li and T. Zhang, *Nat. Commun.*, 2019, **10**, 1–10.

30   C. H. Hu, C. Chizallet, C. Mager-Maury, M. Corral-Valero, P. Sautet, H. Toulhoat and P. Raybaud, *J. Catal.*, 2010, **274**, 99–110.

31   M. C. Valero, P. Raybaud and P. Sautet, *J. Phys. Chem. B*, 2006, **110**, 1759–1767.

32   J. Lee, E. J. Jang and J. H. Kwak, *Appl. Catal. A Gen.*, 2019, **569**, 8–19.

33   S. A. Chambers, T. Droubay, D. R. Jennison and T. R. Mattsson, *Science (80-.).*, 2002, **297**, 827–831.

34   Y. Kwon, T. Y. Kim, G. Kwon, J. Yi and H. Lee, *J. Am. Chem. Soc.*, 2017, **139**, 17694–17699.

35   H. V. Thang and G. Pacchioni, *ChemCatChem*, 2020, **12**, 2595–2604.

36   R. Addou, T. P. Senftle, N. O'Connor, M. J. Janik, A. C. T. Van Duin and M. Batzill, *ACS Nano*, 2014, **8**, 6321–6333.

37   H. V. Thang, S. Tosoni, L. Fang, P. Bruijnincx and G. Pacchioni, *ChemCatChem*, 2018, **10**, 2634–

2645.

38   H. V. Thang, G. Pacchioni, L. DeRita and P. Christopher, *J. Catal.*, 2018, **367**, 104–114.

39   X. Ye, C. Yang, X. Pan, J. Ma, Y. Zhang, Y. Ren, X. Liu, L. Li and Y. Huang, *J. Am. Chem. Soc.*, 2020, **142**, 19001–19005.

40   Y. Fujimori, W. E. Kaden, M. A. Brown, B. Roldan Cuenya, M. Sterrer and H. J. Freund, *J. Phys. Chem. C*, 2014, **118**, 17717–17723.

41   G. S. Parkinson, Z. Novotny, G. Argentero, M. Schmid, J. Pavelec, R. Kosak, P. Blaha and U. Diebold, *Nat. Mater.*, 2013, **12**, 724–728.

42   G. Eranna, B. C. Joshi, D. P. Runthala and R. P. Gupta, *Crit. Rev. Solid State Mater. Sci.*, 2004, **29**, 111–188.

43   J. Ye, C. Liu, D. Mei and Q. Ge, *ACS Catal.*, 2013, **3**, 1296–1306.

44   J. Ye, C. Liu and Q. Ge, *J. Phys. Chem. C*, 2012, **116**, 7817–7825.

45   H. Hartnagel, A. L. Dawar, C. Jagadish and A. K. Jain, *Semiconducting transparent thin films*, CRC Press, 1995.

46   A. Von Weber and S. L. Anderson, *Acc. Chem. Res.*, 2016, **49**, 2632–2639.

47   A. Von Weber, E. T. Baxter, H. S. White and S. L. Anderson, *J. Phys. Chem. C*, 2015, **119**, 11160–11170.

48   A. Von Weber, E. T. Baxter, S. Proch, M. D. Kane, M. Rosenfelder, H. S. White and S. L. Anderson, *Phys. Chem. Chem. Phys.*, 2015, **17**, 17601–17610.

49   G. Kresse and J. Furthmüller, *Phys. Rev. B - Condens. Matter Mater. Phys.*, 1996, **54**, 11169–11186.

50   G. Kresse, *J. Non. Cryst. Solids*, 1995, **192**–**193**, 222–229.

51   P. E. Blöchl, *Phys. Rev. B*, 1994, **50**, 17953–17979.

52   J. P. Perdew, K. Burke and M. Ernzerhof, *Phys. Rev. Lett.*, 1996, **77**, 3865–3868.

53   M. Marezio, *Acta Crystallogr.*, 1966, **20**, 723–728.

54   H. J. Monkhorst and J. D. Pack, *Phys. Rev. B*, 1976, **13**, 5188–5192.

55   D. J. Wales and J. P. K. Doye, *J. Phys. Chem. A*, 1997, **101**, 5111–5116.

56   G. Sun, A. N. Alexandrova and P. Sautet, *J. Chem. Phys.*, 2019, **151**, 194703.

57   M. Mizuhashi, *Thin Solid Films*, 1980, **70**, 91–100.

58   E. H. Morales, Y. He, M. Vinnichenko, B. Delley and U. Diebold, *New J. Phys.*, 2008, **10**, 125030.

59   D. Silber, P. M. Kowalski, F. Traeger, M. Buchholz, F. Bebensee, B. Meyer and C. Wöll, *Nat.*

Commun., 2016, **7**, 1–6.

60　M. Wagner, P. Lackner, S. Seiler, A. Brunsch, R. Bliem, S. Gerhold, Z. Wang, J. Osiecki, K. Schulte, L. A. Boatner, M. Schmid, B. Meyer and U. Diebold, *ACS Nano*, 2017, **11**, 11531–11541.

61　T. Bauer, T. Schmaltz, T. Lenz, M. Halik, B. Meyer and T. Clark, *ACS Appl. Mater. Interfaces*, 2013, **5**, 6073–6080.

62　D. Matthey, J. G. Wang, S. Wendt, J. Matthiesen, R. Schaub, E. Lægsgaard, B. Hammer and F. Besenbacher, *Science (80-.).*, 2007, **315**, 1692–1696.